

Controllable structuring of exciton-polariton condensates in cylindrical pillar microcavities

V.K. Kalevich^{1,2}, M.M. Afanasiev^{1,2}, V.A. Lukoshkin^{1,2}, D.D. Solnyshkov³, G. Malpuech³,
K.V. Kavokin^{1,2}, S.I. Tsintzos⁴, Z. Hatzopoulos⁵, P.G. Savvidis^{4,6}, and A.V. Kavokin^{1,7}

¹*Spin Optics Laboratory, State University of Saint-Petersburg,*

1 Ulianovskaya, 198504 St-Petersburg, Russia

²*Ioffe Institute, Russian Academy of Sciences,*

26 Politechnicheskaya, 194021 St-Petersburg, Russia

³*Insitut Pascal, Photon-N2, Clermont Université,*

CNRS and University Blaise Pascal,

24 avenue des Landais, 63177 Aubiere cedex, France

⁴*IESL-FORTH, P.O. Box 1527, 71110 Heraklion, Crete, Greece*

⁵*Department of Physics, University of Crete, 71003 Heraklion, Crete, Greece*

⁶*Department of Materials Science and Technology,*

University of Crete, 71003 Heraklion, Crete, Greece and

⁷*Physics and Astronomy School, University of Southampton,*

Highfield, Southampton SO171BJ, United Kingdom

Abstract

We observe condensation of exciton polaritons in quantum states composed of concentric rings when exciting cylindrical pillar GaAs/AlGaAs microcavities non-resonantly by a focused laser beam normally incident at the center of the pillar. The number of rings depends on the pumping intensity and the pillar size, and may achieve 5 in the pillar of $40\text{ }\mu\text{m}$ diameter. Breaking the axial symmetry when moving the excitation spot away from the pillar center leads to transformation of the rings into a number of bright lobes corresponding to quantum states with nonzero angular momenta. The number of lobes, their shape and location are dependent on the spot position. We describe the out-of-equilibrium condensation of polaritons in the states with different principal quantum numbers and angular momenta with a formalism based on Boltzmann-Gross-Pitaevskii equations accounting for repulsion of polaritons from the exciton reservoir formed at the excitation spot and their spatial confinement by the pillar boundary.

PACS numbers: 71.36.+c, 73.20.Mf, 78.45.+h, 78.67.-n

I. INTRODUCTION.

Exciton-polaritons are mixed light-matter quasiparticles that appear due to exciton-photon coupling in semiconductor crystal structures [1, 2]. They are composite bosons and demonstrate characteristic bosonic effects, in particular, stimulated scattering [3] and Bose-Einstein condensation [4, 5]. These effects are at the origin of polariton lasing which is manifested by spontaneous generation of coherent and monochromatic light by a many-body coherent state: condensate of exciton-polaritons [6, 7]. Polariton lasers are promising for applications in opto-electronics and information technologies [8]. From the point of view of fundamental physics, they represent a unique laboratory for studies of coherent many-body quantum systems. The microscopic size of polariton condensates (typically, $0.01 \div 0.1$ mm) allows studying their shapes by optical spectroscopy methods. Another important aspect of polariton condensation is that it does not necessarily take place in the ground state. Very clear evidences of polariton condensation in excited states were given in Refs. [9–11]. The non-resonant optical pumping creates an excitonic reservoir localized under the excitation spot. In the mean-field approximation, the interactions of excitons from the reservoir and exciton-polaritons from the condensate may be accounted for by introducing an effective repulsive potential acting upon the polaritons [10, 12, 13], which pushes polaritons away from the pump spot. Exploiting this effect, in the recent years, several groups reported shaping of polariton condensates in optical traps [14, 15], strain induced traps [16], laterally patterned microcavity structures realized by etching [10, 17–19], or metal deposition [20, 21]. A pattern formation in exciton-polariton condensates has been observed by several groups [18, 22, 23]. In particular, formation of ring condensates with large angular momenta has been demonstrated in etched rings microcavities [24] and using optically created confining potentials [23]. The same type of optical potential has been used to create polariton condensates with large angular momenta which led to the formation of the “Abrikosov like” vortex chain [25]. Ring-shape condensates of exciton-polaritons attract a specific interest as they are promising for generation of non-dissipative Bessel-Gaussian light beams [26] and may be used for Mach-Zehnder, Sagnac [24] or Aharonov-Bohm type interferometry [27] and for studies of the vortex lattice dynamics [25].

Recently, we have reported an observation of ring-shape condensates in cylindrical pillar microcavities [28]. The rings were formed due to repulsion of the polaritons from the

excitonic reservoir created in the central part of the pillar by non-resonant optical excitation. Together with the quantum confinement potential provided by the pillar boundary, this optically induced repulsive potential governs the shape of polariton condensates. The eigenmodes in the cylindrical potential of an empty pillar are typically characterized by a radial quantum number which sets the number of rings visible in an experiment, and an angular momentum quantum number setting the number of lobes which can appear on the rings. Of course, the exact shape of the condensate wave function depends on the shape of the effective potential induced by the exciton reservoir, on its position in the real space and on the strength of the interaction between polaritons. The radial and angular-momentum quantum numbers can be used to characterize the polariton condensate state in the majority of cases. Here we show that, tuning the diameter of the pillar, intensity and position of the pumping beam, one can achieve a remarkable degree of control over these quantum numbers, which fully govern the shape of polariton condensates. In particular, we demonstrate the formation of condensates composed by multiple concentric rings where the excitation spot is at the center of the pillar. The number of rings is set by the diameter of the pillar and the pumping intensity and may be varied between 1 and 5 in our experiments. Furthermore, the formation of condensates in a superposition of states with large angular momentum magnitude, i.e. the absolute value of its projection on the structure axis, has been achieved by shifting the excitation spot from the center of the pillar. The condensate in this case splits into a number of lobes which are symmetrically distributed on a ring. When the pumping spot is strongly shifted away from the pillar center, the cylindrical symmetry of the potential seen by the condensate is fully broken and the condensate forms a pattern reminding a “heart” pictogram. These drastic modifications of the shape of the wave-functions of polariton condensates are fully controllable. We have modelled the system with Boltzmann-Gross-Pitaevskii equations [19] which takes into account pumping, decay, energy relaxation and the spatial profile of the condensate wave function in the potential created by the pillar, the cloud of non-condensed excitons and the condensate itself. A good agreement between theory and experiment has been obtained.

This paper is organized as follows. In Sec. II we describe the sample and the experimental setup. The experimental results are presented in Sec. III, where we demonstrate a dramatic dependence of the polariton-condensate pattern on the diameter of the pillar, pumping power and the position of the excitation spot. The theoretical model, results of calculation and

their comparison with the experiment are presented in Sec. IV. The summary of our findings is given in Sec. V.

II. SAMPLE AND SETUP

We studied a set of cylindrical pillars which were etched from a planar $5\lambda/2$ AlGaAs distributed Bragg reflector microcavity. The measured quality factor is $Q = 16000$. Four sets of three 10 nm GaAs quantum wells (QWs) are placed at the antinodes of the cavity electric field to maximize the exciton-photon coupling [29]. The microcavity wedge allowed scanning across the sample to set the detuning energy $\delta = E_C - E_X$, where E_C and E_X are energies of the cavity mode and of the heavy-hole exciton at zero in-plane wavevector ($k = 0$). The photoluminescence (PL) of the pillar was non-resonantly excited by a cw Ti:sapphire laser tuned to the local minimum of the upper stop-band of the distributed Bragg reflector (≈ 110 meV above E_X). The laser beam was focused to a $2\mu\text{m}$ spot by a microscope objective (numerical aperture = 0.42). The same objective was used to collect the PL signal. Real space images as well as the k -space images of pillars were projected on the entrance $100\mu\text{m}$ slit of a 50 cm-monochromator and, after spectral dispersion, were recorded by a cooled CCD-camera. When taking real space and k -images without spectral dispersion, the grating of the monochromator was set to the zeroth order of diffraction, and the width of the entrance slit was set to 3 mm. All experiments were performed at normal incidence of the excitation beam on the sample. A cut-off interference filter was installed in front of the entrance slit to suppress the excitation laser light scattered from the pillar surface. The sample under study was kept in the helium-flow cryostat at $T = 3.5$ K.

We studied pillars with the diameters of 25, 30, and $40\mu\text{m}$. The pillars chosen for this study are characterized by a negative photon-exciton detuning $\delta = -(0.5 \div 3.5)$ meV. We have found no strong qualitative dependence of the observed effects on the detuning in the limited range of detunings we have examined.

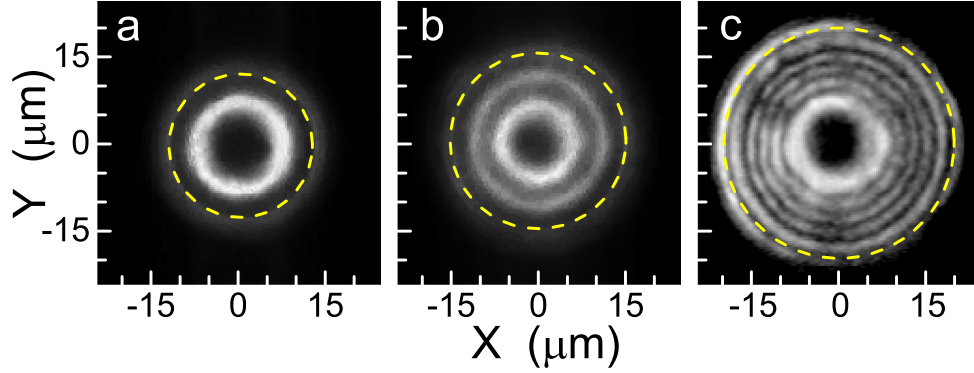


FIG. 1. Real-space images of (a) 25, (b) 30 and (c) 40 μm pillars under nonresonant excitation into the center of the pillar. The excitation energy $h\nu_{\text{exc}} = 1.664\text{ eV}$, pumping power $P \approx 1.5P_{\text{th}}$, $T = 3.5\text{ K}$. Dashed circumferences show pillar edges.

III. EXPERIMENTAL RESULTS

A. Splitting of polariton condensate into concentric rings

Figure 1 presents real-space images of the (a) 25, (b) 30 and (c) 40 μm pillars obtained under sharply focused nonresonant excitation at the center of the pillar using a pumping power 1.5 times higher than the polariton condensation threshold (an example of experimental determination of the condensation threshold P_{th} is given below, see the discussion of Fig. 9). Every image represents a set of concentric rings, the number of which increases with the increase of the pillar diameter. The inner diameter of the outer ring in every pillar coincides with that of the pillar top shown by the dashed circumference. In Figures 1a and 1b the outer ring emission is much weaker than the emission of the inner rings. The spectral analysis of the real-space images in Fig. 1, similar to one described in detail in the Ref. [28] for the 25 μm pillar, shows that the outer ring is due to the emission of heavy-hole excitons, which escapes from the side surface of the pillar. Thus, the outer ring is not related to the condensate, so that the number of condensate rings seen in the Fig. 1 amounts to 1, 2 and 5 for the pillars of the diameter of 25, 30 and 40 μm , respectively.

In order to make sure that each of the inner rings belongs to a single condensate, we have performed the Young interferometry measurements, as described in Ref. [28]. The coherence in each of the two inner rings in the 30 μm pillar has been checked by measuring the interference pattern from the spots marked by small circles 1–4 in Fig. 2a. The images of spots 1

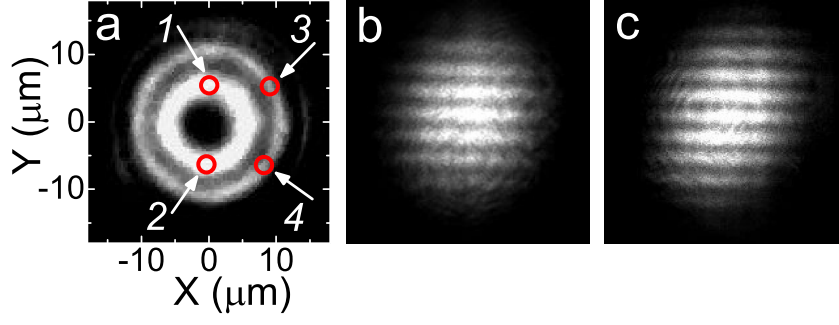


FIG. 2. (Color online) (a) Real-space image of $30\text{ }\mu\text{m}$ pillar under optical excitation into the center of the pillar and the Young interferometry patterns obtained by superimposing the light beams emitted by spots (b) 1–2 and (c) 3–4. $P/P_{\text{th}} \approx 2$.

and 2 for the smaller ring and of spots 3 and 4 for the larger ring have been superimposed on the detector using a supplementary lens. The corresponding fringe patterns are clearly seen in the interferometry images shown in Figs. 2b and 2c. This observation confirms the buildup of spatial coherence in every ring of the fragmented polariton condensate.

The number of rings we observe in micro-PL has been found to depend on the diameter of the pillar and the pumping power. As a general rule, the higher the pumping power the lower is the number of rings. This can be seen in Fig. 3, which demonstrates the reduction of the number of the rings in emission of the $40\text{ }\mu\text{m}$ pillar from 5 to 1, as the pump power increases from $1.6P_{\text{th}}$ to $11P_{\text{th}}$. One can see that the ring of the smallest diameter has the

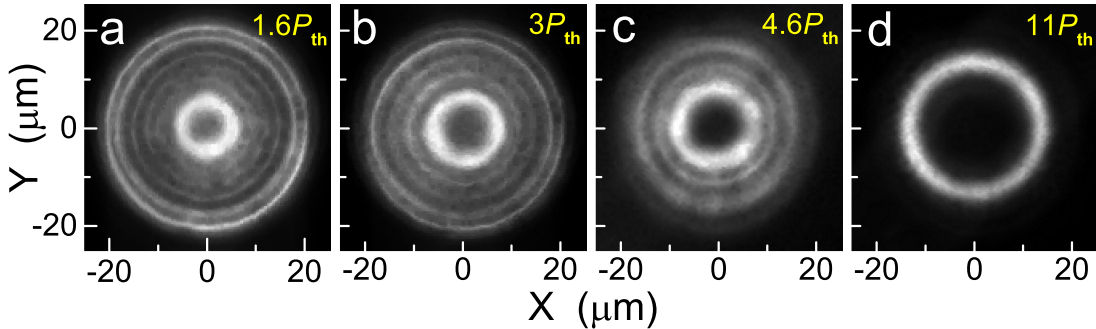


FIG. 3. Transformation of 5 rings into one with the pumping power increase. The micro-PL images are obtained under excitation into the center of $40\text{ }\mu\text{m}$ pillar. $P/P_{\text{th}} = 1.6$ (a), 3 (b), 4.6 (c) and 11 (d).

highest brightness (Figs. 3a–c). As the pumping intensity increases, the diameter of this ring increases as well (approximately, from 10 to 25 μm), and simultaneously the rings of larger diameters disappear one by one. This is a result of the increase both of the height of the potential induced by the cloud of uncondensed excitons and of the polariton relaxation rate. Indeed, close to the threshold the condensation takes place in excited states, while far above threshold it takes place in the ground state of the potential trap formed by the pump and the pillar boundary. The evolution of polariton condensates towards the ground state with the pump intensity increase is a general feature reported in several previous publications [10, 11, 17, 19].

B. Azimuthal structuring of the condensate

Once we shift the pump spot slightly away from the center of the pillar, the axial symmetry of the potential seen by the polariton condensates appears to be broken. As a consequence, the condensate rings transform into periodic sequences of bright lobes as can be

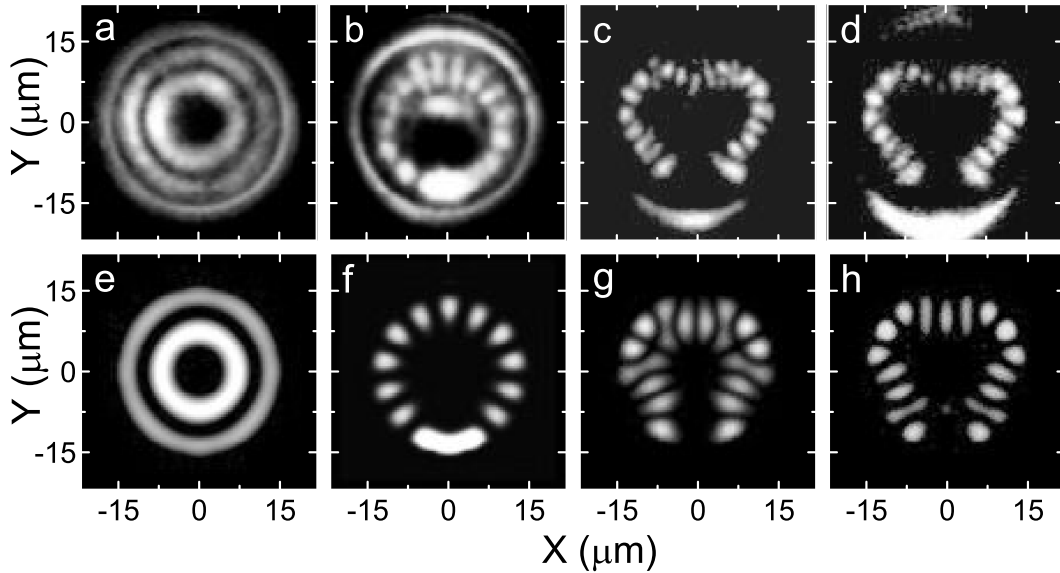


FIG. 4. Experimental (a–d) and calculated (e–h) real-space images of 30 μm pillar at different shifts of the excitation spot downwards from the pillar center. The shift is equal to 0 (a, e), 3 μm (b, f), 9 μm (c, g), and 13 μm (d, h). $P/P_{\text{th}} = 1.7$.

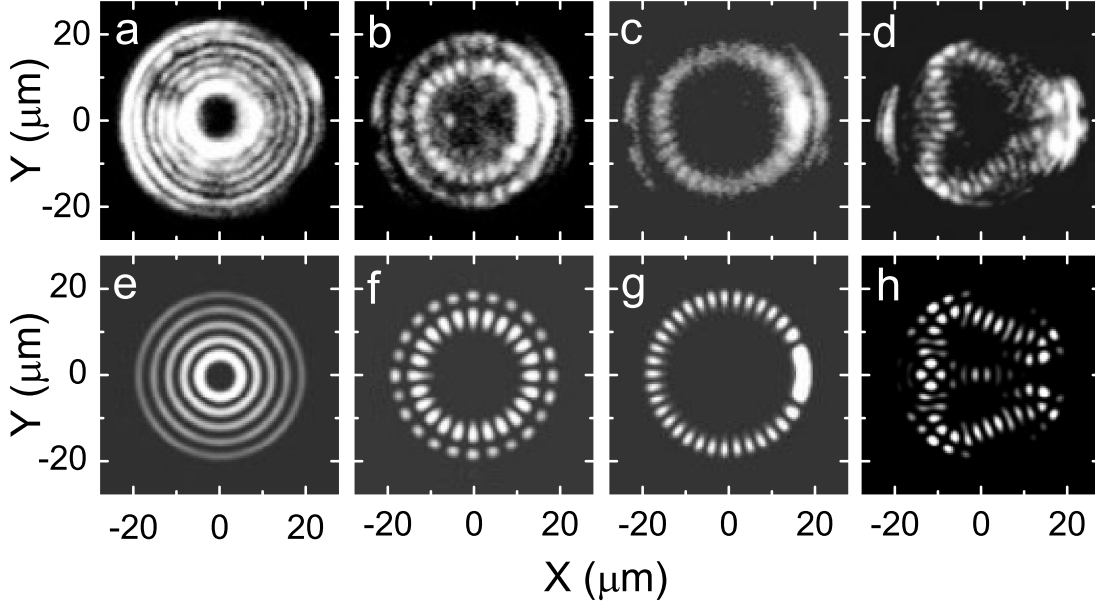


FIG. 5. Experimental (a–d) and calculated (e–h) real-space images of the polariton condensates in the $40\,\mu\text{m}$ pillar at different shifts of the excitation spot to the right from the pillar center. The shift is equal to 0 (a, e), $5\,\mu\text{m}$ (b, f), $10\,\mu\text{m}$ (c, g), and $17\,\mu\text{m}$ (d, h). $P/P_{\text{th}} \approx 1.5$.

seen in Figs. 4 and 5 for the pillars of $30\,\mu\text{m}$ and $40\,\mu\text{m}$ diameters, respectively.

Figure 4 shows spatially resolved PL images of the $30\,\mu\text{m}$ pillar excited slightly above the polariton condensation threshold for different pump spot positions. One can see that the two concentric rings, observed when exciting at the center of the pillar (Fig. 4a), transform into a set of well-resolved lobes (Fig. 4b–d). If the shift of the excitation spot from the center of the pillar is small ($3\,\mu\text{m}$), these lobes still form a ring (Fig. 4b), while if the excitation spot is shifted further towards the pillar edge, they form a complex pattern (Figs. 4c, d), which reminds a pictogram of heart.

Even more complex lobe patterns have been observed in a $40\,\mu\text{m}$ pillar, as Fig. 5 shows. Five uniform rings, observed when exciting in the center of the pillar (Fig. 5a), transform into two rings of lobes (Fig. 5b), which merge to form a single ring of lobes (Fig. 5c) as the pump spot shifts by 5 and $10\,\mu\text{m}$ from the center of the pillar, respectively. The further shift of the pump spot towards the pillar edge ($17\,\mu\text{m}$ shift in Fig. 5d) results in the redistribution of the lobes which now form the picture of a fly with its head oriented towards the pump spot.

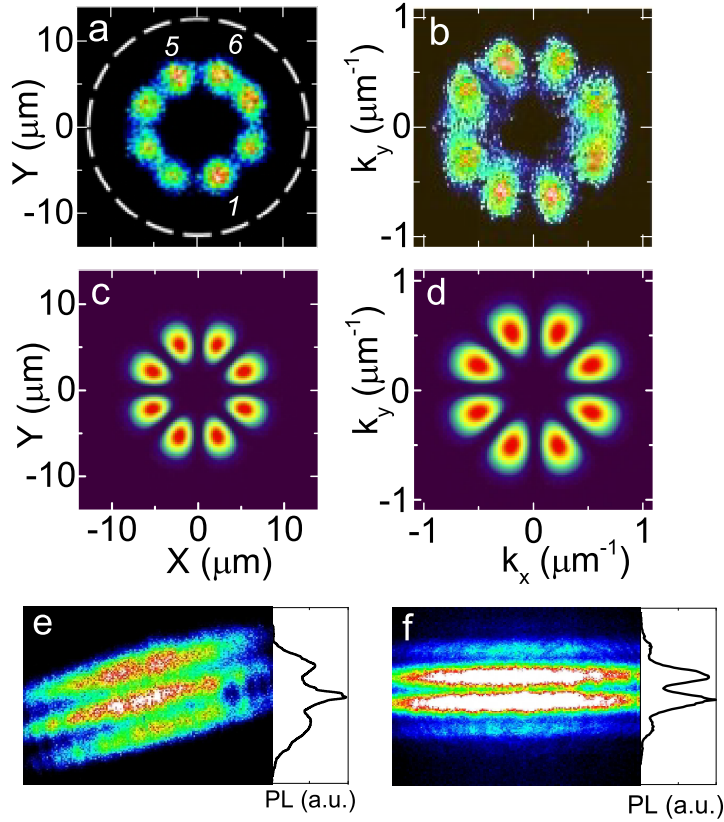


FIG. 6. (Color online) Splitting of the polariton condensate into 8 lobes observed in (a) real-space and (b) k -space images of a $25\,\mu\text{m}$ pillar at the shift of $\sim 1\,\mu\text{m}$, $P/P_{\text{th}} \approx 1.7$. (c) and (d) are calculated real-space and k -space images. (e, f) are Young interferometry patterns obtained by superimposing light emitted by lobes (e) 1 and 5 and (f) 1 and 6. Right insets in figures (e) and (f) present PL intensity profiles at the centers of the interference images (e) and (f).

It is important to check the spatial coherence of the condensate split into many lobes. We have performed the Young interferometry measurements in a $25\,\mu\text{m}$ pillar, where 8 clearly distinguishable lobes separated by sufficiently large distances have been observed (Figs. 6a and 6b). Simulations of the polariton and exciton dispersions in the model of three coupled oscillators (not shown here) yield the detuning value of $\delta = -3\,\text{meV}$ in this particular pillar. The pillar with a smaller diameter has been chosen for these measurements as it shows larger lobes separated by larger distances as compared to 30 and $40\,\mu\text{m}$ pillars. The experimental real-space images as well as k -space images, taken in the $25\,\mu\text{m}$ pillar for a very small (not exceeding $1\,\mu\text{m}$) displacement of the pump spot from the center, show 8 nearly identical

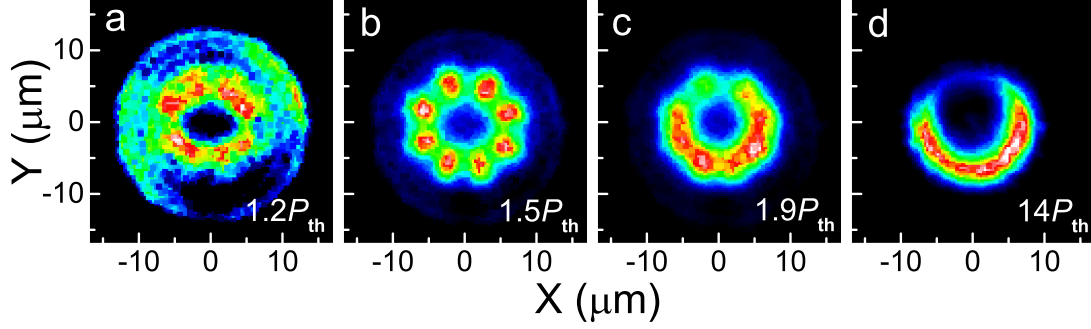


FIG. 7. (Color online) Transformation of 8 lobes into a crescent with the increase of the excitation power in a $25\,\mu\text{m}$ pillar. P/P_{th} is equal to 1.2 (a), 1.5 (b), 1.9 (c) and 14 (d).

lobes distributed symmetrically on one ring. Note that the maxima of emission of each of the 8 lobes in the k -space image in Fig. 6b correspond to the observation angle of about 6 degrees (for details see below the discussion of Figs. 7 and 8). Thus, the emission of the lobe condensate in the far field range is composed by 8 beams, oriented at small ($\sim 6^\circ$) oblique angles with respect to the axis of the structure.

The Young interferometry has been realized by combining the magnified real space images of two lobes passing through two $50\,\mu\text{m}$ holes in a screen placed between the sample and the detector. In panels (e) and (f) in Fig. 6 one can see the Young interferometry patterns obtained by superimposing light beams emitted by lobes 1 and 5 and 1 and 6, respectively. Very clear interference patterns seen in these images confirm the spatial coherence of the observed lobe condensate. Right insets in panels (e) and (f) present PL intensity profiles at the centers of the interference images (e) and (f). The intensity profile in the inset (e) has a maximum in its center, while the similar profile in the inset (f) has a minimum in its center. Clearly, the interference of the lobes 1 and 5 is constructive, while the interference of the lobes 1 and 6 is destructive. This means that the lobes 1 and 5 are in phase, while the lobes 1 and 6 are in anti-phase. We have checked in a similar way (not shown here), that the lobes 1 and 4 have opposite phases as well. This proves that the nearest neighboring lobes are in the anti-phase. Having in mind the even number of lobes in Fig. 6a, one can conclude that the wave-function of the condensate on a ring is nothing but a standing wave resulting from the interference between two waves rotating in clockwise and counterclockwise directions, in agreement with Ref. [23].

The lobe condensate pattern is very sensitive to the excitation power as one can see in

Fig. 7 presenting the real space images of polariton lasing from the $25\text{ }\mu\text{m}$ pillar taken at different pump powers. The formation of the lobes is starting from the pump powers just above the polariton condensation threshold (Fig. 7a). The further increase of pumping intensity results in a formation of a very clear and symmetric image constituted by 8 equidistant and almost identical lobes (Fig. 7b). The further pumping power increase makes lobes to merge (Fig. 7c) and, eventually, to form a crescent pattern (Fig. 7d).

To obtain the energy spectrum of the above mentioned condensate, we have measured the energy dependence of the angular distribution of the polariton emission as a function of the pumping power for the position of the pump spot at the surface of the pillar corresponding to the formation of a condensate containing 10 lobes. We have focused the k -space image of the condensate to the entrance $100\text{ }\mu\text{m}$ slit of the monochromator, in such a way that the slit passed through the centers of two lobes situated most closely to the vertical axis crossing the center of the condensate image in the k -space. The width of the angular distribution of emission measured in this way is different by no more than by 5% from one that would have been measured along the diameter.

The polariton dispersion curves, measured in this way, are shown in Fig. 8. At the pumping power below the condensation threshold, the polariton dispersion exhibits a minimum at 1.536 eV and $k = 0$ (Fig. 8a). A broad emission line at 1.543 eV is interpreted as the PL of heavy-hole excitons coming from the side surface of the pillar due to the Rayleigh scattering of light at the imperfections of this surface, as we have already found [28] when exciting into the pillar center. This edge emission is responsible for the outer rings observed in Fig. 1.

The increase of the excitation power above the condensation threshold results in an abrupt narrowing of the distribution of polariton emission as a function of energy and angle, down to fractions of meV and a couple of angular degrees as can be seen in Figures 8 b–f. This effect is a fingerprint of polariton condensation. We remind that, if the excitation spot is placed at the center of this pillar, the condensation in a single ring takes place. The corresponding reciprocal space emission [28] is localized around $k = 0$. When the excitation spot is slightly moved away, as we show here, the emission just above threshold is composed by the peak at $k = 0$ and two supplementary maxima, at the detection angles of 6.5° , and the energy exceeding the bottom of the low polariton branch by about 0.3 meV (Fig. 8b). The intensity of the supplementary peaks in Figure 8 rapidly increases with the increase of the pumping power, so that they dominate the central peak at $P = 1.7P_{\text{th}}$ and $P = 2.1P_{\text{th}}$,

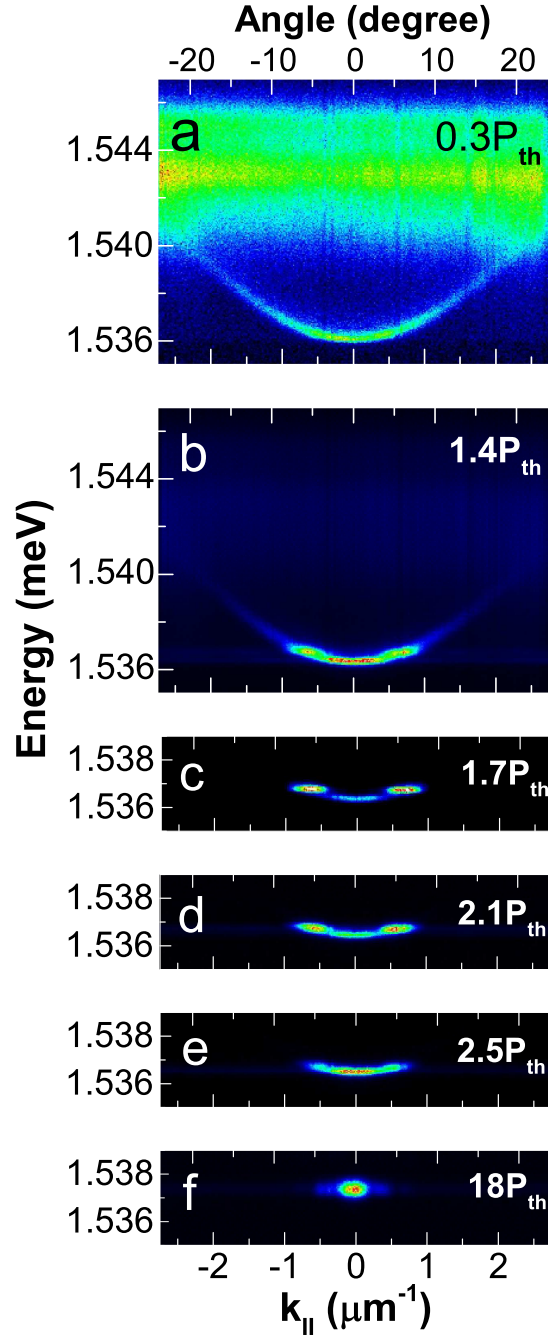


FIG. 8. (Color online) Exciton-polariton dispersion curves in the 25 μm pillar taken at different excitation powers and at the shift of the excitation spot from pillar center corresponding to the observed 10 lobes. $h\nu_{\text{exc}} = 1.662 \text{ eV}$, $T = 3.5 \text{ K}$, $\delta = -3 \text{ meV}$. The brightness in each image is normalized to its maximum.

as one can see in the Fig. 8c and Fig. 8d, respectively. This observation is correlated with the real space images shown in Figure 7. Just above threshold, the lobe structure is partly hindered by the presence of other energy states, whereas it fully dominates around $1.5P_{\text{th}}$. At $P = 2P_{\text{th}}$ the supplementary maxima start approaching each other (Fig. 8d) and they merge eventually at $P = 2.5P_{\text{th}}$ (Fig. 8e). The further pumping increase until $P = 18P_{\text{th}}$ leads to the decrease of the angular width of emission down to $\approx 2.5^\circ$ (Fig. 8f), whereas in real space, the lobes disappear. These data allow visualizing the passage from out-of-equilibrium exciton-polariton condensation in the excited states just above threshold to the condensation in the ground energy state of the potential imposed by the exciton cloud and the pillar boundary.

Figure 9 presents the detailed power dependences of the main parameters extracted from the polariton PL spectra measured in the $25\mu\text{m}$ pillar at the same shift of the excitation spot as in Fig 8. The dependence of the integrated PL intensity on the pumping intensity is shown in Fig. 9a. It demonstrates a very strong nonlinear increase. The PL intensity rises by two orders of magnitude when the excitation power is only doubled, from 3 to 6 mW. The threshold behavior of the PL intensity is a signature of the polariton condensation regime. The threshold power found from this curve is equal to $P_{\text{th}} = 2.8\text{ mW}$ (shown by the vertical arrow in panel a).

Figure 9b shows the energies of the polariton ground state ($k = 0$, circles) and of the lobe condensate (diamonds). It is seen that the lobe condensate exists within the narrow range of pumping powers, approximately from 3 to 7 mW, which is hatched in Fig. 9. Its energy is nearly constant throughout this power range. At the same time, the ground state energy of exciton-polaritons monotonously increases, reproducing the well-known blue shift induced by the exciton-exciton interaction [9, 30, 31]. Note that the range of existence of the lobe condensate largely coincides with the range of the superlinear growth of the PL intensity in Fig. 9a.

Spectral widths (FWHM) of the emission of a single lobe (open squares) and of the integral emission of the polariton gas outside the condensate (full squares) are also shown in Fig. 9b. The spectral width of the lobe condensate varies slowly with the pump power and remains close to 0.3 meV. On the contrary, the emission of the non-condensed polariton gas is characterized by a much larger (1.2 meV) spectral width. The remarkable (four-fold) narrowing of the radiation spectrum when approaching P_{th} also evidences the realization of

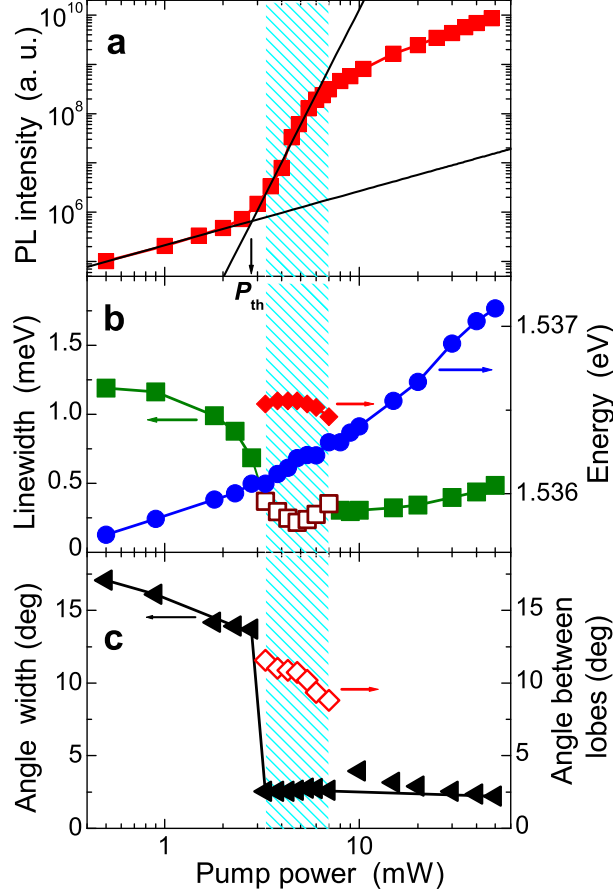


FIG. 9. (Color online) Dependences of (a) integrated intensity, (b) energy and spectral width (squares) and (c) angular width of polariton PL (triangles) and angle between the angle-resolved emission maxima corresponding to two opposite lobes (diamonds) on the pump power in the $25 \mu\text{m}$ pillar at such a shift ($\sim 1 \mu\text{m}$) of excitation spot from the pillar center that 10 lobes are observed. Diamonds in panel (b) show PL peak energies of the lobes, while circles present polariton ground state energy. Vertical arrow in panel (a) shows the threshold of polariton stimulated emission $P_{th} = 2.8 \text{ mW}$. Solid lines are guides for the eye.

the polariton condensation regime at $P > P_{th}$.

The full width at half maximum (FWHM) of the angular-resolved polariton emission as well as the angle between the emission maxima of two separate lobes in k -space are shown in Fig. 9c by triangles and diamonds, respectively. The angular width of a single lobe is given for the range of existence of the lobe condensate. One can see that at $P > P_{th}$ the angular width decreases abruptly, from 13.5 to 2.5 degrees. At the same time, the angle

between the emission maxima of two separate lobes with the opposite lateral components of the wave vector exhibits little changes, decreasing steadily from 11.5° to 9° . Thus, we observe all the characteristic features of polariton lasing: the superlinear growth of intensity and strong narrowing of spectral and angle distributions as well as the blue shift of the polariton emission above the lasing threshold.

IV. THEORETICAL MODEL, RESULTS OF CALCULATION AND COMPARISON WITH THE EXPERIMENTAL DATA

Theoretical simulations of polariton relaxation and condensation in micropillars were carried out using the model based on coupled semi-classical Boltzmann equations and the Gross-Pitaevskii equation, solved in a self-consistent way. At each time step, a stationary Gross-Pitaevskii equation is solved in order to find the current wave functions of the polariton condensate in the pillar, taking into account the quantum confinement due to the edges of the pillar and the effective potential created due to the exciton-exciton interactions between the reservoir and the condensate as well as between polaritons in the condensate. Neglecting spin, this equation can be written as

$$E_{i,t_j} \Psi_{i,t_j} = -\frac{\hbar^2}{2m} \Delta \Psi_{i,t_j} + (\alpha \eta \rho_R(x, y) N_R(t_j) + \alpha \eta^2 \sum_i |\Psi_{i,t_j}|^2 n_{i,t_j} + V) \Psi_{i,t_j} . \quad (1)$$

Here, E_{i,t_j} are the eigenenergies and Ψ_{i,t_j} are the many-body wave functions (normalized to unity) at the fixed time moment t_j , m is the polariton effective mass, V is the micropillar confinement potential, $\alpha = 6E_b a_B^2$ is an estimate of the exciton-exciton interaction constant describing the repulsion of exciton polaritons from the exciton reservoir and from each other, η is the exciton fraction of the considered quantum state, E_b is the exciton binding energy, a_B is the exciton Bohr radius, $\rho_R(x, y)$ is the normalized reservoir density, N_R is the number of particles in the reservoir and n_{i,t_j} is the number of particles in each quantum state.

Then, the scattering rates are calculated accounting for the overlap between the reservoir and the wave functions found in the previous step. The relaxation mechanisms taken into account are both exciton-exciton and exciton-phonon scattering. Exciton-exciton scattering is the most important for the transfer of quasiparticles between the reservoir and the quantized polariton states, because the energy difference in this case is large, while exciton-phonon scattering is responsible for the relaxation between the quantized states

of the condensate, because the energy difference between these states is small, and their populations are relatively low as well.

As shown previously [19], due to the thermal distribution of excitons in the reservoir, the exciton-exciton interaction leads to the thermalization of the polariton states in a similar fashion to the exciton-phonon interaction. The reservoir is modelled as a single state with a population $N_R(t_j) = n_R(E = 0, t_j)Sm_Xk_BT/2\pi\hbar^2$ (here m_X is the exciton mass, S is the normalization surface, n_R is the occupation of the corresponding reservoir state), whose thermal distribution is accounted for in the scattering rates. The shape of the reservoir, given by the function $\rho_R(x, y)$, is defined by the spatial location and shape of the pump spot (the exciton diffusion is assumed to be slow).

The semi-classical Boltzmann equations for the quantized polariton states matching the stationary Gross-Pitaevskii equation can be written as:

$$\begin{aligned} \frac{dn_i}{dt} = & -\frac{n_i}{\tau_i} - n_i \sum_k (W_{XX}I_{ikRR}N_R + W_{XP}^{ik})(n_k + 1) \begin{pmatrix} 1, & k < i \\ e^{-E_{ik}/k_BT}, & k > i \end{pmatrix} \\ & + (n_i + 1) \sum_k (W_{XX}I_{ikRR}N_R + W_{XP}^{ik}I_{ik})n_k \begin{pmatrix} e^{-E_{ik}/k_BT}, & k < i \\ 1, & k > i \end{pmatrix}, \quad (2) \\ & + (W_{XX}I_{iRRR}N_R + W_{XP}^{iR}I_{iR}) \left(N_R(n_i + 1) - n_i \frac{Sm_Xk_BT}{2\pi\hbar^2} e^{-E_{iR}/k_BT} \right) \end{aligned}$$

where $I_{ikRR}, I_{ik}, I_{iRRR}, I_{iR}$ are the overlap integrals defined below, τ_i is the lifetime of the respective state.

For the reservoir state, the equation reads:

$$\frac{dN_R}{dt} = P - \frac{N_R}{\tau_R} - \sum_i (W_{XX}I_{iRRR}N_R + W_{XP}^{iR}I_{iR}) \times \left(N_R(n_i + 1) - \frac{n_i Sm_Xk_BT}{2\pi\hbar^2} e^{-E_{iR}/k_BT} \right). \quad (3)$$

Here P is the non-resonant pumping populating the reservoir, $\tau_R = 400$ ps, W_{XX} is the exciton-exciton scattering rate, which is a fitting parameter of the model, and $W_{XP}^{ik,R} = W_{XP} \exp[-(E_i - E_{k,R})a_B/\hbar c\pi]$ is the exciton-phonon scattering rate between the corresponding states, W_{XP} is another fitting parameter. The details on the derivation of these equations are given in Ref. [19].

All scattering rates are affected by the corresponding overlap integrals, which change with time together with the shape of the quantized wave functions, according to the Gross-Pitaevskii equation. The dimensionless overlap integrals are defined as follows: $I_{ikRR} = S^3 \int |\psi_i^* \psi_k|^2 \rho_R^2 dx dy$, $I_{iRRR} = S^3 \int |\psi_i|^2 \rho_R^3 dx dy$. The overlap integrals obtained by summation of scattering rates with different phonon wavevectors read: $I_{ik} = S \int |\psi_i^* \psi_k|^2 dx dy$, $I_{iR} = S \int |\psi_i|^2 \rho_R dx dy$. These overlap integrals are of a significant importance, because they define relative scattering efficiencies for different quantized polariton states.

The results of the simulations reproducing the experimental data are shown in the theoretical panels of Figures 4, 5, 6. Depending on the size of the pillar, the calculated shapes of the condensates are different, but the agreement with the experiment is always good.

Figure 4 presents the results of theoretical simulations of the shapes of polariton condensates compared with the experimental data for a $30 \mu\text{m}$ pillar (panels e–h). The transition between the states with zero angular momentum (panel e) and high angular momentum magnitude is obtained (panel f) by breaking of the cylindrical symmetry due to the pump spot displacement. At large displacements (panels g, h), the state of the condensate can be interpreted as two opposite polariton flows generated at the pumping spot and reflected at the pillar boundary, while the center of the pillar remains empty because of the destructive interference of outgoing and incoming flows.

Figure 5 presents the calculated shapes of polariton condensates for the $40 \mu\text{m}$ pillar (panels e–h). In the case of centrosymmetric excitation, the condensate is formed in the quantum state with the principal quantum number 5 (panel e). The violation of the cylindrical symmetry leads again to the excitation of the quantum states having higher angular momentum magnitude (panels f, g). At the strong displacement (panel h), the propagation of polaritons away from the pumping spot and around the pillar is observed again, in a similar fashion to the $30 \mu\text{m}$ pillar.

In larger pillars, the quantum confinement energy is smaller, so that the greater number of polariton modes having different quantum numbers can be excited simultaneously. This is why only 2 rings are observed in the $30 \mu\text{m}$ pillar and 5 rings are observed in the $40 \mu\text{m}$ pillar. The polariton lasing threshold for all these modes is achieved approximately at the same pumping intensity. At the strong displacement, both in the $30 \mu\text{m}$ pillar and in the $40 \mu\text{m}$ pillar, the theoretical simulation shows the asymmetric pattern of lobes reminding a heart pictogram, in a full qualitative agreement with the experiment.

Figures 6c and 6d show simulations of the exciton-polariton condensate in the smallest, $25\text{ }\mu\text{m}$ pillar. For this pillar, a small displacement of the pumping spot leads to the formation of an 8-lobe state (the principal quantum number 1, the orbital quantum number 4). Panel (c) shows the real space image, and panel (d) shows the reciprocal space image of this state, corresponding to the experimental panels (a), and (b), respectively. The image of the condensate in the reciprocal state reflects the symmetry of the image in the real space. The absence of a maximum in the center of the reciprocal space image clearly shows that this state is different from the ground state, where the condensate forms at higher pumping power, as shown in Figure 8 and reproduced in the simulations (not shown).

The main conclusions of this theoretical section can be summarized as follows. Because of the close polariton lasing threshold powers for several nearly degenerate polariton modes, the condensation may occur not only in the thermodynamically favorable ground state, but sometimes in the higher-energy states, whose profile is defined mostly by the repulsive potential of the localized reservoir. The lowest energy state is strongly repelled by the reservoir and has a lower overlap integral with it, which is why the scattering into this state is strongly suppressed. At the same time, higher energy states have larger overlap integrals, but these states experience also depletion due to the exciton-phonon scattering towards the lower energy states. Depending on the conditions, the condensation may start in a single state or in several quantum states. In the latter case, at the pumping power just exceeding the lasing threshold, the condensate occupies several discrete energy levels. The further increase of the pumping power leads to accumulation of particles in the lowest energy state because of the scattering rate enhancement by bosonic stimulation. This tendency is experimentally seen in Fig. 8.

V. CONCLUSIONS

We have demonstrated an efficient optical control of the shape of exciton-polariton condensates and switching between different topologies of the condensates in cylindrical micropillars. Switching between multi-ring condensates and patterns of lobes is achieved by shifting the excitation spot by fractions of a micron from the pillar center. Such a strong sensitivity of polariton condensates to the location of the excitation spot may be understood in terms of switching between nearly degenerate polariton states characterized by different

radial and orbital quantum numbers. A small perturbation is sufficient to start condensation in a different quantum state. Bosonic condensation in several excited states and pumping-dependent redistribution of bosons in the real space are characteristic of driven dissipative bosonic systems, such as polariton lasers. These results demonstrate remarkable flexibility of wave function engineering in polariton lasers. Multi-ring condensates have a high potentiality for realization of Bessel-Gauss non-diffractive light beams. The structuring of polariton condensates, their fragmentation, formation of multiple lobes and various spatial patterns open way to realization of bosonic intergrated circuits and logic gates.

ACKNOWLEDGMENTS

The work of VKK, MMA, VAL, KVK and AVK was financially supported by the Russian Ministry of Education and Science (Contract No.11.G34.31.0067). PGS acknowledges financial support from FP7 EU ITN “INDEX” 289968 and IRSES “POLATER” exchange grants and Greek GSRT ARISTEIA program Apollo. DDS and GM acknowledge the support of ANR “QUANDYDE” and EU “POLAPHEN” projects.

-
- [1] V.M. Agranovich and V.L. Ginzburg, *Crystal Optics with Spatial Dispersion and Excitons* (Springer-Verlag, New York, 1984).
 - [2] J.J. Hopfield, Phys. Rev. **112**, 1555 (1958).
 - [3] P.G. Savvidis, J.J. Baumberg, R.M. Stevenson, M.S. Skolnick, D.M. Whittaker, and J.S. Roberts, Phys. Rev. Lett. **84**, 1547 (2000).
 - [4] J. Kasprzak, M. Richard, S. Kundermann, A. Baas, P. Jeambrun, J.M.J. Keeling, F.M. Marchetti, M.H. Szymańska, R. André, J.L. Staehli, V. Savona, P.B. Littlewood, B. Deveaud, and Le Si Dang, Nature **443**, 409 (2006).
 - [5] R. Balili, V. Hartwell, D. Snoke, L. Pfeiffer, and K. West, Science **316**, 1007 (2007).
 - [6] A. Imamoglu, R.J. Ram, S. Pau, and Y. Yamamoto, Phys. Rev. A **53**, 4250 (1996).
 - [7] S. Christopoulos, G. Baldassarri, Höger von Högersthal, A.J.D. Grundy, P.G. Lagoudakis, A.V. Kavokin, J.J. Baumberg, G. Christmann, R. Butté, E. Feltin, J.-F. Carlin, and N. Grandjean, Phys. Rev. Lett. **98**, 126405 (2007).

- [8] A.V. Kavokin, Nature Photon. **7**, 591 (2013).
- [9] D. Bajoni, P. Senellart, E. Wertz, I. Sagnes, A. Miard, A. Lemaître, and J. Bloch, Phys. Rev. Lett. **100**, 047401 (2008).
- [10] E. Wertz, L. Ferrier, D.D. Solnyshkov, R. Johne, D. Sanvitto, A. Lemaître, I. Sagnes, R. Grousson, A.V. Kavokin, P. Senellart, G. Malpuech and J. Bloch, Nature Phys. **6**, 860 (2010).
- [11] E. Wertz, A. Amo, D.D. Solnyshkov, L. Ferrier, T.C.H. Liew D. Sanvitto, P. Senellart, I. Sagnes, A. Lemaître, A.V. Kavokin, G. Malpuech, and J. Bloch, Phys. Rev. Lett. **109**, 216404 (2012).
- [12] M. Wouters, I. Carusotto, and C. Ciuti, Phys. Rev. B **77**, 115340 (2008).
- [13] G. Christmann, G. Tosi, N.G. Berloff, P. Tsotsis, P.S. Eldridge, Z. Hatzopoulos, P.G. Savvidis, and J.J. Baumberg, Phys. Rev. B **85**, 235303 (2012).
- [14] G. Tosi, G. Christmann, N.G. Berloff, P. Tsotsis, T. Gao, Z. Hatzopoulos, P.G. Savvidis and J.J. Baumberg, Nature Phys. **8**, 190 (2012).
- [15] A. Askitopoulos, H. Ohadi, A.V. Kavokin, Z. Hatzopoulos, P.G. Savvidis, and P.G. Lagoudakis, Phys. Rev. B **88**, 041308(R) (2013).
- [16] G. Liu, D.W. Snoke, A. Daley, L. Pfeiffer, and K. West, arXiv:1402.4339.
- [17] V.G. Sala, D.D. Solnyshkov, I. Carusotto, T. Jacqmin, A. Lemaître, H. Terças, A. Nalitov, M. Abbarchi, E. Galopin, I. Sagnes, J. Bloch, G. Malpuech, and A. Amo, arXiv:1406.4816.
- [18] L. Ferrier, E. Wertz, R. Johne, D.D. Solnyshkov, P. Senellart, I. Sagnes, A. Lemaître, G. Malpuech, and J. Bloch, Phys. Rev. Lett. **106**, 126401 (2011).
- [19] M. Galbiati, L. Ferrier, D.D. Solnyshkov, D. Tanese, E. Wertz, A. Amo, M. Abbarchi, P. Senellart, I. Sagnes, A. Lemaître, E. Galopin, G. Malpuech, and J. Bloch, Phys. Rev. Lett. **108**, 126403 (2012).
- [20] C.W. Lai, N.Y. Kim, S. Utsunomiya, G. Roumpos, H. Deng, M.D. Fraser, T. Byrnes, P. Recher, N. Kumada, T. Fujisawa, and Y. Yamamoto, Nature **450**, 529 (2007).
- [21] R. Brückner, A.A. Zakhidov, R. Scholz, M. Sudzius, S.I. Hintschich, H. Fröb, V.G. Lyssenko and K. Leo, Nature Photon. **6**, 322 (2012).
- [22] F. Manni, K.G. Lagoudakis, T.C.H. Liew, R. André, and B. Deveaud-Plédran, Phys. Rev. Lett. **107**, 106401 (2011).

- [23] A. Dreismann, P. Cristofolini, R. Balili, G. Christmann, F. Pinsker, N.G. Berloff, Z. Hatzopoulos, P.G. Savvidis, and J.J. Baumberg, Proceedings of the National Academy of Sciences of the United States of America **111**, 8770 (2014).
- [24] C. Sturm, D. Tanese, H.S. Nguyen, H. Flayac, E. Galopin, A. Lemaître, I. Sagnes, D. Solnyshkov, A. Amo, G. Malpuech, and J. Bloch, Nat. Commun. **5**, 3278 (2014).
- [25] T. Boulier, H. Terças, D.D. Solnyshkov, Q. Glorieux, E. Giacobino, G. Malpuech, and A. Bramati, arXiv:1405.1375.
- [26] C. Ryu, K.C. Henderson, and M.G. Boshier, New J. Phys. **16**, 013046 (2014).
- [27] I.A. Shelykh, G. Pavlovic, D.D. Solnyshkov, and G. Malpuech, Phys. Rev. Lett. **102**, 046407 (2009).
- [28] V.K. Kalevich, M.M. Afanasiev, V.A. Lukoshkin, K.V. Kavokin, S.I. Tsintzos, P.G. Savvidis, and A.V. Kavokin, J. Appl. Phys. **115**, 094304 (2014).
- [29] P. Tsotsis, P.S. Eldridge, T. Gao, S.I. Tsintzos, Z. Hatzopoulos, and P.G. Savvidis, New J. Phys. **14**, 023060 (2012).
- [30] D. Bajoni, E. Semenova, A. Lemaître, S. Bouchoule, E. Wertz, P. Senellart, and J. Bloch, Phys. Rev. B **77**, 113303 (2008).
- [31] M. Vladimirova, S. Cronenberger, D. Scalbert, K.V. Kavokin, A. Miard, A. Lemaître, J. Bloch, D. Solnyshkov, G. Malpuech, and A. V. Kavokin, Phys. Rev. B **82**, 075301 (2010).